Julian Frei, Max Biegler, Michael Rethmeier, Christoph Böhne, Gerson Meschut

Investigation of liquid metal embrittlement of dual phase steel joints by electro-thermomechanical spot-welding simulation

This is an Accepted Manuscript of an article published by Taylor & Francis in Science and Technology of Welding and Joining on February 22, 2019, available online: http://www.tandfonline.com/10.1080/13621718.2019.1582203.

Frei, Julian; Biegler, Max; Rethmeier, Michael; Böhne, Christoph; Meschut, Gerson (2019). Investigation of liquid metal embrittlement of dual phase steel joints by electro-thermomechanical spot-welding simulation. Science and Technology of Welding and Joining, 24(7), 624–633. https://doi.org/10.1080/13621718.2019.1582203

Investigation of liquid metal embrittlement of dual phase steel joints by electro-thermomechanical spot-welding simulation

Julian Frei[1], +49 30 39006-364, julian.frei@ipk.fraunhofer.de, ORCID: 0000-0003-3924-4881

Max Biegler[1], +49 30 39006-404, max.biegler@ipk.fraunhofer.de, ORCID: 0000-0001-8665-5347

Michael Rethmeier[123], +49 30 8104-1550, michael.rethmeier@bam.de

Christoph Böhne[4], +49 5251 / 60 49 16, christoph.boehne@lwf.upb.de

Gerson Meschut[4], +49 5251 / 60 30 31,

gerson.meschut@lwf.uni-paderborn.de

[1]*Joining Technology, Fraunhofer Institute for Production Systems and Design Technology, Berlin, Germany*

[2]*Welding Technologies, Federal Institute for Materials Research and Testing (BAM), Berlin, Germany*

[3]*Institute for Machine Tools and Factory Management (IWF), Technical University of Berlin, Germany*

[4]*Laboratory for Material and Joining Technology (LWF®), Paderborn, Germany*

Investigation of liquid metal embrittlement of a dual phase steel joints by electro-thermomechanical spot-welding simulation

Abstract

A 3D electro-thermomechanical model is established in order to investigate liquid metal embrittlement. After calibration to a dual phase steel of the 1000 MPa tensile strength class, it is used to analyse the thermo-mechanical system of an experimental procedure to enforce liquid metal embrittlement during resistance spot welding. In this procedure, a tensile stress level is applied to zinc coated advanced high strength steel samples during welding. Thereby, liquid metal embrittlement formation is enforced, depending on the applied stress level and the selected material. The model is suitable to determine and visualise the corresponding underlying stresses and strains responsible for the occurrence of liquid metal embrittlement. Simulated local stresses and strains show good conformity with experimentally observed surface crack locations.

Keywords: RSW, LME, advanced high strength steel, zinc coated steel, testing method, dual phase steel, cracking, electro-thermomechnical model

Introduction

Over the past 30 years, the use of advanced high strength steels (AHSS) in automotive production has been constantly rising, while resistance spot welding (RSW) still is the most common joining process in body-in-white production [1]. AHSS combine good formability with higher strength levels compared to common steel grades, which allows the realization of lightweight concepts [2].

Due to the higher strength of these steels, higher restraints are induced along the process chain, e.g. as a consequence of increased springback after bending [3], potentially affecting the tendency of these steels to develop surface cracks [4]. Another aspect, that influences the weldability of AHSS, is the zinc coating, commonly applied for corrosion protection. Both the presence of zinc and the mechanical load affect the cracking susceptibility of steels [5], occasionally provoking a phenomenon called liquid metal embrittlement (LME) [6]. LME is currently observed in the industry during RSW, and is therefore subject of present research [7]. While LME was observed on some AHSS grades initially, it is also observed on other steel types, like high-strength low-alloy steels presently [8]. Investigated for more than 100 years already, LME is not only limited to welding, but a variety of high temperature processes (e.g. hot forming) [9]. It can be described as the loss of ductility of an otherwise ductile metal in the presence of another metal in liquid state [6]. Three main circumstances have been identified to be necessary for LME crack formation: tensile stresses, a susceptible solid metal, and a molten metal [6]. The role of compressive stresses, which may increase the LME susceptibility by promotion of zinc diffusion, is not thoroughly investigated yet [10].

There is a variety of liquid metal/solid metal systems prone to LME, e.g. Al_{solid}/Ga_{liquid} or Cu_{solid}/Hg_{liquid} [11], including the system $Steel(Fe)_{solid}/Zn_{liquid}$. Auger and Laurang [12] link the propagation of the brittle crack to the continuous supply with

liquid metal. When no liquid remains to be sucked towards the crack tip by capillary effects, the brittle crack stops, either completely, or changes to ductile fracture mode depending on the experimental conditions.

The contact between the solid metal and the liquid metal influences the LME susceptibility. It is described by the grain boundary energy γ_{GB} and interface energy γ_{SL} between solid and liquid. Common grain boundary penetration takes place if

$$\gamma_{GB} \geq 2\gamma_{SL} \quad (1)$$

is fulfilled [13].

LME can be enforced by an experimental procedure, during which tensile stresses are applied to a sample, shaped similar to a typical flat tensile specimen during welding [7]. To analyse the LME susceptibility of steels, the thermo-mechanical mechanism within the material is of great interest. However, reliable data is not accessible with common measuring techniques. Furthermore, a wide range of factors must be considered, some of which are constantly varying, like electrode wear, ambient temperature, coating thickness, etc. Finite element simulation provides a powerful tool to investigate the underlying mechanisms of the thermo-mechanical system, revealing among others the resulting stresses, strains and temperature fields. Disturbance variables can be excluded or kept constant.

In the literature, finite element methods have been frequently used to study RSW processes in great detail [14]. To resolve the inter-dependency of electric flow, thermal heating and mechanical contacts, nonlinear electro-thermomechanical approaches are commonly chosen in either 2- or 3-dimensional formulations, depending on the studied phenomena: Huh et al. [15] present a 3-dimensional thermo-electrical model with temperature dependent thermophysical, as well as electrical material data, to study the effect of different electrode shapes on nugget shapes and sizes. Feulvarch et al. [16] use

a 2-dimensional electro-thermomechanical model for a 3-sheet stack up and validate the nugget shape with cross sections. Wink et al. [17] investigate temperature dependent material properties such as bulk resistivity and plastic flow behaviour and establish a numerical RSW model to study softening during welding in press-hardening steels. Pakkanen et al. [18] develop a 2-dimensional numerical spot welding simulation model for AHSS and validate it with cross sections as well as drill-hole residual stress measurements. As LME-cracking occurs not only in the middle plane of the nugget, a 3-dimensional simulation approach is chosen in this work to resolve temperature and stress-fields around the weld.

The development of the electrical resistivity during the process is of great interest to correctly model the heat generation and nugget formation: Babu et al. [19] present an empirical-analytical model to evaluate temperature- and pressure-dependent contact resistance and find a high influence of surface roughness. In another publication, Rogeon et al. [20] show that the contact resistance is also dependent on the surface condition (coated or uncoated), and provide detailed, temperature-dependent data. With the higher contact pressures present in a typical spot weld, they also show that contact resistance remains almost constant over the temperature range in a typical process. This behaviour is confirmed by Wang et al. [21]: They model the bulk- and contact resistivity during welding and find a strong decrease in the contact resistivity upon starting the weld and an almost constant behaviour afterwards. The bulk resistivity, on the other hand, is observed to increase strongly with rising temperatures and becomes predominant. The contact resistivity remains constant during the process, and only changes due to the increasing contact area as the electrodes sink into the material. The bulk resistivity is implemented in a temperature dependent manner to account for its strong rise during the process.

Besides the mechanical, thermal and electrical components, phase transformations play a major role during spot welding: Iyota et al. [22] investigated the influence of thermal strains and changed material behaviour due to martensitic transformation in a 2-dimensional electro-thermomechanical spot welding model. They found a large influence of material transformations on the residual stresses after welding and observed good agreement between their numerically simulated stresses and x-ray diffraction measurements.

LME cracking is governed by tensile stresses, susceptible microstructure and grain boundary penetration by liquid metal alloying elements in steels. For a holistic, multiscale approach, length scales of nanometers (grain boundaries) as well as millimetres (external loads and structural model) would have to be considered. This study focuses on the latter scale, based on the hypothesis that LME susceptibility for a specific material class can be modelled via a macroscropic model, relying on temperature, stresses and strains. Grain boundary weakening by liquid zinc is regarded as a constant boundary condition and not included in the simulation. This approach is computationally feasible and considered appropriate for industrial use.

Materials and methods

Materials

The framework project of this study includes a variety of AHSS materials of different strength classes, to evaluate for LME susceptibility. These steels were secured and characterized by WorldAutoSteel, the global automotive steel producer consortium with 22 member companies. For the calibration of the material model, a dual phase steel of the strength class 1000 MPa (hereinafter called DP1000) with a yield strength of 750 MPa, and an ultimate tensile strength of 1010 MPa is used as a basis. The sheet

thickness is 1.5 mm. The material is commonly used in car body manufacturing.

Methods

Welding under external load

The welding under external load procedure enforces LME cracking of zinc-coated AHSS materials by applying a tensile stress field to a sample during spot welding [7], thereby creating extreme welding conditions. The stress field is induced hydraulically by a simple experimental setup as shown in Figure 1, and can be adjusted to different load levels according to the materials' mechanical properties. The initially applied stress is not adjusted during welding, but a preloading only. As a result value, the total crack length on the sample surface is measured optically (by aid of image editing software) after chemical removal of the zinc layer. The level of tensile stress necessary to reproducibly provoke LME cracking can be determined by incremental increase of the applied stress for a testing material, e.g. in 10 % steps of the material's $R_{p0.2}$.

Resistance measurement

The measurements of the contact resistances are performed based on ISO 18594, for force levels from 1 kN to 5 kN. For each measurement, two steel sheets the size of 100 mm x 50 mm are used to carry out eight measurements in total at distinct spots on the sheets. A constant current is then applied, and the voltage drop (between the upper electrode and the additional contacts) is measured, allowing a calculation of the partial resistance for each stage. Accompanying measurements of the system resistance are executed before and after each test series along with the periodical polishing and cleaning of the electrodes.

Validation experiments

Validation experiments are conducted using a servo-mechanical C-type welding gun and a medium frequency inverter power source, used in constant current regulation. F1-16-20-5.5 flat type electrode caps according to ISO 5821 [23] are used. A welding current range (WCR) is determined for the testing material. Two different welding currents, and two electrode forces are chosen for validation. The welding time is kept constant at 380 ms, hold and squeeze times at 200 ms each. To measure the thermal history, a line of three type K thermocouples is micro-welded to the top sheet (see Figure 2). The thermocouples are located at a distance of approximately 4 mm, 5 mm and 6 mm to the weld center. Based on an assumed electrode indentation diameter of 7.5 mm, these are the closest possible positions. After welding, a macroscopic top view image of the sample is used to determine the exact distances of the thermocouples to the actual weld center. Metallographic cross sections are used for comparing the indentation depth and weld nugget size/shape.

Numerical Simulation

The numerical simulations of the spot welding process are carried out with the commercial welding simulation software simufact.welding 7.2. A 3D coupled electro-thermo-mechanical structural welding simulation model with included phase transformation is set up in the software to reproduce the spot welding process as closely as possible. The model consists of 14,556 linear hexahedral elements with a selective 2-fold refinement in the weld zone leading to an edge length of 0.3 mm and a refined element count of 23,684. A mesh convergence study for 3-fold refinement resulted in 3.1 % change in the peak process temperatures and was discarded due to long calculation times. On a workstation equipped with two 8-core Intel Xeon E5-2667

CPUs, solving the model with 2-fold refinement took 1.8 h. Initially, the mechanical model is solved to reproduce the closing of the electrodes and clamping forces. With the electrode/sheet and sheet/sheet contact areas established, the first electrical increment is calculated. The analysis comprising of electrical, thermal and mechanical steps in each increment is weakly coupled, i.e. the thermal increment has no feedback to the electrical increment and the mechanical increment has no feedback to the thermal increment within a single time step.

Electrical analysis. The electrical field E is related to the current density J in the conductor based on Ohm's law by

$$J = \sigma E \tag{2}$$

where σ is the conductivity of the conductor. The electrical field strength can be calculated with the electrical potential V:

$$E = -grad(V) \tag{3}$$

With the assumption that there is no additional current source

$$div(J) = 0 \tag{4}$$

The electro-kinetic equation is constituted from equations (1-3)

$$div(\sigma \cdot grad(V)) = 0 \tag{5}$$

Finally, the heat generation Q due to the current flow is calculated through Joule heating

$$Q = J^2 \cdot R \tag{6}$$

With the temperature dependent resistance matrix R. [24]

Thermal analysis. After each electrical increment, a thermal increment for heat transfer is calculated. The governing heat transfer differential equation is written as: [25]

$$\rho C_p \frac{dT}{dt} = -\nabla \cdot q(r,t) + Q(r,t) \quad (7)$$

Where ρ is the density, C_p is the specific heat capacity, T is the Temperature and t is the time. The relative reference coordinate is denoted as r, Q is the heat source as determined from the electrical analysis and q the heat flux vector, expressed as

$$q = -\lambda \nabla T \quad (8)$$

With the thermal conductivity λ. Convective and radiative boundary conditions are applied to all free surfaces. The convective heat transfer is written as

$$Q_C = -hA(T_1 - T_2) \quad (9)$$

h is the convective heat transfer coefficient in W/(m²K), A denotes the convective surface, T_1 is the surface temperature and T_2 the temperature of the surrounding air.

At the clamped boundaries, the sample is in contact with steel surfaces. For these contacts, a higher heat loss is modelled through an expression like Eq. (8). The convective heat transfer coefficient is replaced with a contact heat transfer coefficient with a value of 500 W/(m²K) to simulate the strong, temperature-dependent heat flow into the metallic parts of the clamping.

According to the temperatures, heating- and cooling rates, the phase distribution is calculated after the thermal analysis. Above Ac_3 temperature, the material is considered to be fully austenitic. During cooling, all phases that became austenitic are transformed into martensite below 500 °C. This simplification is valid due to the large heating and

cooling rates in spot welding and was used for instance in [22].

Mechanical analysis. A mechanical increment based on an elasto-plastic formulation is calculated after each thermal increment. The nonlinear analysis of stresses and distortions is based on the thermal strains generated through localised expansion and contraction of the materials. These strains cause local, inhomogeneous elastic and plastic material behaviour, which, in turn, generates the stresses and distortions. The mechanical stress equilibrium equation is written as: [25]

$$\nabla \cdot \sigma = 0 \tag{10}$$

Where σ denotes the stress tensor. The mechanical constitutive law can be written as

$$\sigma = C\varepsilon_e \tag{11}$$

$$\varepsilon = \varepsilon_e + \varepsilon_p + \varepsilon_T \tag{12}$$

C is the stiffness tensor and ε is the total-, ε_e the elastic-, ε_p the plastic and ε_T the thermal-strain tensor. Temperature dependent values for the mechanical and thermal parameters k, λ, C_p, the elastic modulus E, the yield strength σ_y, and the plastic flow behaviour have to be defined in the material properties input and are discussed in the results section. Material plastic- and stress-history is set to zero as the material heats above solidus temperature (1400 °C) to model stress relaxation due to liquefaction of the steel.

All process times as well as the clamping boundary conditions are modelled to match the experiments. The sheets are supported by bearings in the model that prevent "falling" but allow for in-plane motion as well as detachment. To reduce the model complexity, some assumptions are made: The material properties are temperature

dependent but changes in phase only affect the materials yield strength and plastic flow behaviour. The density and Poisson's ratio are constant and the influence of the mechanical deformations on the temperature field is considered to be negligible. The weld pool is modelled as a low-stiffness solid and the occurrence of weld pool dynamics is neglected.

Results

Material parameters

Especially for AHSS that have been introduced recently, temperature dependent material data for welding simulation are not widely available and their experimental acquisition is costly and time-consuming. For this publication, the parameters are acquired from a mixture of literature sources and targeted experiments. The thermophysical properties of a 600 MPa strength class dual phase steel are determined experimentally by Schwenk et al. [26], shown in Figure 3. The assumption is made, that the data remains the same for different strength classes of dual phase steels. The same assumption is made for the thermomechanical material data, i.e. that the young's modulus remains at ~210 GPa at room temperature, and the softening with heat remains equal. The temperature dependent thermal expansion coefficient remains unchanged. The simplification is made, that only the yield strength and ultimate tensile strength must be scaled for different grades of the same material class. The flow behaviour is also determined by Schwenk for DP600 [27] from room temperature up to 800 °C and can be scaled to the yield strength of 750 MPa and an ultimate tensile strength of 1010 MPa to mimic the DP1000 steel. This approach is already demonstrated in [18]. To correctly account for compression occurring during spot welding, the data is extended manually by flow curves with progressively lower flow stresses until solidus

temperature. In addition, phase dependent data for plastic flow is necessary for the austenitic phase in the high temperature range as well as for the martensitic phase forming during cooling. Both data sets are not readily available for DP1000 steels in the literature. Therefore, data determined by Wink et al. [17] for austenitic and martensitic phases of a press-hardening 22MnB5 steel are taken. The electrical bulk resistivity is determined in relation to temperature in the same publication by Wink et al. [17].

The electrical contact resistivity is strongly dependent on steel grades, coatings and electrode forces [28]. Figure 4 shows the determined values for electrode/sheet and sheet/sheet resistances for clamping forces between 1 kN and 5 kN. While the contact resistances change strongly for low force levels, they remain almost constant at the high forces relevant for RSW and are in a similar range as the values determined in [19], if the contact area of the electrodes is taken into account. In accordance with the publication by Rogeon et al. [20], the contact resistance is kept constant over the temperature.

Model validation

With the simplifications regarding material parameters, a thorough calibration of the model has to be conducted. The calibration is done in three stages: First temperatures are measured during welding using thermocouples and compared to experiments for deviations in peaks and cooling behaviour (see Figure 5). Subsequently, metallographic cross sections are prepared and the weld nugget size and shape are compared, shown in Figure 6.

LME investigation

The model is applied to investigate conditions which cause LME cracking, by simulating the welding under external load procedure. The external tensile stress level

necessary to reproducibly enforce LME cracking of the testing material was determined experimentally to be 60 % of the material's $Rp_{0.2}$. Figure 7 shows the typical LME initiation site of a welding under external load sample in top view. Without externally applied tensile stresses, i.e. under standard welding conditions, the material does not exhibit LME. With lower external stress levels, only occasional LME is observed. Figure 8 shows the simulation model of the welding under external load procedure. For reduction of calculation time, only the middle part of the tensile sample is modelled. A welding parameter set is chosen according to [29]: electrode force is 4.5 kN, weld time 380 ms. While the right side of the sample is fixed, a tensile force is applied to the left side, which results in the uni-axial stress field shown in Figure 8, corresponding to 60 % of the material's yield strength. This value is determined experimentally to be required to reproducibly enforce LME. The simulative replication of the experimentally determined loadcase is an easy and effective way to determine and visualise local stress and strain values during the RSW process responsible for LME formation.

Figure 9 shows the effective stress distribution in top view at various time steps of the welding process in top view. Areas adjacent to the electrode indentation have been identified experimentally to be the main sites of LME formation, and are therefore in focus for evaluation of the simulation [10]. Thermally induced tensile stresses mainly form during cooling due to shrinking of material. After cooling down close to room temperature, local stress maxima up to approximately 800 MPa are observed. During heating, in the highly heated/molten area, little to no stresses can be transferred, which leads to a redistribution of the initial tensile stress field towards the outer areas of the sample (top left). Excessive tensile stresses are transformed into plastic strain. Subsequently, necking of the sample is visible at the sample's outer edges. The

significant stress pattern shown in the last frame (bottom right) forms during the cooling process, after 5 seconds. Values of approximately 800 MPa are reached in areas which have cooled down near room temperature. The effective stress at the edge of the electrode indentation (so-called 'shoulder', indicated by arrow in Figure 7), where LME typically occurs as, divides into the three components of the triaxial stress state: radial stress (σ_x), circumferential stress (σ_y) and through thickness tress (σ_z). During the simulated procedure, tensile radial and circumferential stresses dominate, as they are supported by the external force applied. In through thickness direction mainly compressive stresses, induced by the electrode, are present.

Figure 10 shows the corresponding effective stress fields in cross section view. The loss of the capability to transfer stresses of the material at high temperatures is clearly visible (top left and right). Furthermore, the stress maxima after cooling are not only present on the surface, but reach down circumferentially around the weld nugget (bottom right).

Figure 11 shows the effective plastic strain which forms during the heating phase of the welding process in top view. It is calculated by integrating incrementally the plastic deformation over time. Although the externally applied force lies in the elastic region initially, the material's mechanical properties deteriorate with increasing temperature. This leads to plastic deformation (PD) and displacement towards the side of the movable clamping. The electrode holds the material underneath it back, while the external load pulls on the adjacent, weakened material. Therefore, the main plastic strain is observed left of the electrode. Surface strains mainly form on the side of applied load, and reach down towards the centre of the weld nugget as can be seen in the cross-section view in Figure 12. Locally, values of 1.5 are reached.

Figure 13 shows the resulting effective plastic strain field (left) and the effective stress field (right) after the welding time at 700 ms, simulated without application of external load. The plastic strain appears less pronounced; maximum values only reach approximately 0.5 locally. The effective stress maximum in the weld center is about 400 MPa. Both stress and strain fields appear symmetrical.

Discussion

The approach for calibration and validation of the material model is proven to be valid for the desired application. FE simulation helps to increase the process understanding of LME significantly, both by calculating values not measurable with conventional techniques and visualizing the results.

The simulation provides in-situ temperature, stress and strain values during welding. These are, amongst other internal/external factors like coating thickness / type [11], grain boundary diffusivity / solubility, or grain boundary energy – interfacial energy relation [30], responsible for LME cracking formation. Evaluation of the resulting stress field shows, that the absolute maximum values on the surface form after significant cooling time of five seconds. Essential for LME formation however, is the presence of zinc in liquid state – which occurs roughly between 420°C and 900°C [31]. As shown in Figure 14, this leads to a critical time range in the simulation between 150 ms and 1800 ms in which the zinc is liquefied on the sample surface.

The maximum stress values on the surface of about 800 MPa (see Figure 8, bottom right) can therefore be disregarded, as they form after this period. A comparison between welding with and without external load (see Figure 9 and Figure 13 left) indicates, that there are higher effective stress values present in the weld center when

external stresses are applied (at typical LME initiation sites approximately 30 % higher). Especially radial and circumferential stresses may facilitate the formation of LME cracks, which are usually arranged in the through-thickness direction. Generally, tensile stresses are regarded as a prerequisite for LME occurrence [13], but their effect on the material's microstructure strongly depends on the local, temperature-dependent material properties [13]. The temperature field is not homogeneous but exhibits large gradients and changes in each time increment. Consequently, this prevents an intuitive evaluation of the simulated stress field. Regarding the PD, the comparison of welding with and without external stresses (Figure 11 and Figure 13 right) shows a local increase of PD by about factor three. The plastic strain field is already calculated in consideration of the temperature-dependency of material properties – it indicates areas, where stresses exceed the temperature-dependent yield strength of the material. The main plastic strains occur within the critical time range, and in an area where LME formation is frequently observed experimentally (see Figure 15). It can therefore be assumed, that PD in combination with the presence of liquid zinc, increases the LME susceptibility generally. Locally, PD values of 1 to 1.5 are reached, which are considered to be critical for LME. Correlation between the PD and the experimentally observed LME locations is found: Figure 14 (right) shows the simulated areas of high PD, and an image extracted from computed tomography of an LME afflicted sample.

Conclusions

An electro-thermomechanical simulation model for investigations on LME of dual phase steels during RSW is established. The validation of the model is successfully conducted; the simplifications made are found to be suitable to simulate the welding process.

The model is applied to investigate the occurrence of LME during RSW. Temperature, stress and strain fields are simulated successfully. A time range is deducted, in which LME can occur due to the presence of liquid zinc. Within this time range, high PD occurs, as the material properties are deteriorated thermally. Global stress maxima, however, form only after significant cooling time and are therefore disregarded. For an effective investigation of the LME susceptibility by use of welding simulation, it is recommended to evaluate the PD rather than effective stresses, as thereby the temperature dependency of material properties is taken into account.

As experiments show, the tested DP1000 material has to be pre-stressed to at least 60 % of its $R_{p0.2}$ in order to reproducibly enforce the formation of LME during RSW. Simulation of strain fields during the welding under external load procedure, at the 60 % $R_{p0.2}$ load level, reveals high local PD values about 1.5 at the surface, correlating with experimentally observed crack locations. Evaluation of the simulated strains during 'normal' welding conditions (i.e. without external load) shows, that the PD here is 2-3 times lower. Under such circumstances, LME, as a result of local strains, is unlikely to occur – provided, that it is not triggered by other internal or external factors.

The established model can be used to simulate other welding parameter or material-thickness combinations, and can be adapted to a wide range of further AHSS materials. It focuses on the in-situ temperature, stress and strain fields of the RSW process, which cannot be measured with conventional techniques. The model is set up on the macroscale, and can therefore not be used to investigate other (especially chemical or intrinsic) aspects of the LME phenomenon.

Acknowledgements

This work was supported by the WorldAutoSteel consortium, and was performed as part of the transnational liquid metal embrittlement in AHSS program.

References

1. Brauser S, Pepke LA, Weber G, Rethmeier M (2010) Deformation behaviour of spot-welded high strength steels for automotive applications. Materials Science and Engineering A 527:7099–7108. doi: 10.1016/j.msea.2010.07.091

2. Pouranvari M, Marashi SPH (2013) Critical review of automotive steels spot welding: process, structure and properties. Science and Technology of Welding and Joining 18:361–403. doi: 10.1179/1362171813Y.0000000120

3. Brauser S, Pepke LA, Weber G, Rethmeier M (2013) Influence of Production-Related Gaps on Strength Properties and Deformation Behaviour of Spot Welded Trip Steel HCT690T. Welding in the World 56:115–125. doi: 10.1007/BF03321342

4. Gaul H, Weber G, Rethmeier M (2011) Influence of HAZ cracks on fatigue resistance of resistance spot welded joints made of advanced high strength steels. Science and Technology of Welding and joining 16:440–446.

5. Frei J, Rethmeier M (2017) Overview and new developments in research on resistance spot welding of advanced high strength steels. In: 5th International Conference on Steels in Cars and Trucks. pp 1–8

6. Joseph B, Picat M, Barbier F (1999) Liquid metal embrittlement: A state-of-the-art appraisal. The European Physical Journal - Applied Physics 15.1:19–31.

7. Frei J, Suwala H, Gumenyuk A, Rethmeier M (2016) Bestimmung der Rissanfälligkeit von hochfesten Stählen beim Widerstandspunktschweißen. Materials Testing 58:7–8. doi: DOI 10.3139/120.110904

8. Milititsky M, Pakalnins E, Jiang C, Thompson AK (2003) On Characteristics of DP600 Resistance Spot Welds. SAE 2003 World Congress & Exhibition. doi: 10.4271/2003-01-0520

9. Nicholas MGG, Old CF (1979) Liquid metal embrittlement. Journal of Materials Science 14:1–18. doi: 10.1007/BF01028323

10. Bhattacharya D (2018) Liquid metal embrittlement during resistance spot welding of Zn-coated high-strength steels. Materials Science and Technology 0:1–21. doi: 10.1080/02670836.2018.1461595

11. Kamdar MH (1983) Liquid Metal Embrittlement. In: Briant CL, Banerji SK (eds) Treatise on materials science and technology. Academic press, pp 361–459

12. Auger T, Lorang G (2005) Liquid metal embrittlement susceptibility of T91 steel by lead– bismuth. Scripta Materialia 52:1323–1328. doi: https://doi.org/10.1016/j.scriptamat.2005.02.027

13. Beal C (2011) Mechanical behaviour of a new automotive high manganese TWIP steel in the presence of liquid zinc. Thesis, Institut national des sciences appliquées de Lyon, France

14. Ashiri R, Haque MA, Ji CW, Shamanian M, Salimijazi HR, Park Y-D (2015) Supercritical area and critical nugget diameter for liquid metal embrittlement of Zn-coated twining induced plasticity steels. Scripta Materialia 109:6–10. doi:

10.1016/j.scriptamat.2015.07.006

15. Huh H, Kang WJ (1997) Electrothermal analysis of electric resistance spot welding processes by a 3-D finite element method. Journal of Materials Processing Technology 63:672–677. doi: 10.1016/S0924-0136(96)02705-7

16. Feulvarch E, Robin V, Bergheau JM (2004) Resistance spot welding simulation: A general finite element formulation of electrothermal contact conditions. Journal of Materials Processing Technology 153–154:436–441. doi: 10.1016/j.jmatprotec.2004.04.096

17. Wink H-J, Krätschmer D (2012) Charakterisierung und Modellierung des Bruchverhaltens von Punktschweißverbindungen in pressgehärteten Stählen Teil II - Simulation des Schweißprozesses. 11. LS-DYNA Forum. Ulm, Germany

18. Pakkanen J, Vallant R, Kičin M (2016) Experimental investigation and numerical simulation of resistance spot welding for residual stress evaluation of DP1000 steel. Welding in the World 60:393–402. doi: 10.1007/s40194-016-0301-4

19. Babu SS, Santella ML, Feng Z, Riemer BW, Cohron JW (2001) Empirical model of effects of pressure and temperature on electrical contact resistance of metals. Science and Technology of Welding and Joining 6:126–132. doi: 10.1179/136217101101538631

20. Rogeon P, Carre P, Costa J, Sibilia G, Saindrenan G (2008) Characterization of electrical contact conditions in spot welding assemblies. Journal of Materials Processing Technology 195:117–124. doi: 10.1016/j.jmatprotec.2007.04.127

21. Wang SC, Wei PS (2001) Modeling Dynamic Electrical Resistance During

Resistance Spot Welding. Journal of Heat Transfer 123:576. doi: 10.1115/1.1370502

22. Iyota M, Mikami Y, Hashimoto T, Taniguchi K, Ikeda R, Mochizuki M (2013) The effect of martensitic transformation on residual stress in resistance spot welded high-strength steel sheets. Journal of Alloys and Compounds 577:S684–S689. doi: 10.1016/j.jallcom.2012.06.109

23. DIN EN ISO 5821:2010 Resistance welding - Spot welding electrode caps. Deutsches Institut für Normung (DIN)

24. Zhang H, Senkara J (2006) Resistance Welding - Fundamentals and Application. Taylor & Francis Group

25. Goldak JA, Akhlaghi M (2005) Computational welding mechanics. Springer Science & Business Media

26. Schwenk C, Rethmeier M (2011) Material properties for welding simulation - measurement, analysis, and exemplary data. Welding Journal 90:220–227.

27. Schwenk C (2007) FE-Simulation des Schweißverzugs lasergeschweißter dünner Bleche - Sensitivitätsanalyse durch Variation der Werkstoffkennwerte. Berlin

28. Harlin N, Jones TB, Parker JD (2003) Weld growth mechanism of resistance spot welds in zinc coated steel. Journal of Materials Processing Technology 143–144:448–453. doi: 10.1016/S0924-0136(03)00447-3

29. SEP 1220-2:2011 Testing and Documentation Guideline for the Joinability of Thin Sheet of Steel - Part 2: Resistance Spot Welding. Stahlinstitut VDEh

30. Razmpoosh MH, Macwan A, Biro E, Chen DL, Peng Y, Goodwin F, Zhou Y (2018) Liquid metal embrittlement in laser beam welding of Zn-coated 22MnB5 steel. Materials & Design 155:375–383. doi: 10.1016/j.matdes.2018.05.065

31. Kim YG, Kim IJ, Kim JS, Chung YI, Choi D-Y (2014) Evaluation of Surface Crack in Resistance Spot Welds of Zn-Coated Steel. Materials Transactions 55:171–175. doi: 10.2320/matertrans.M2013244

Figures

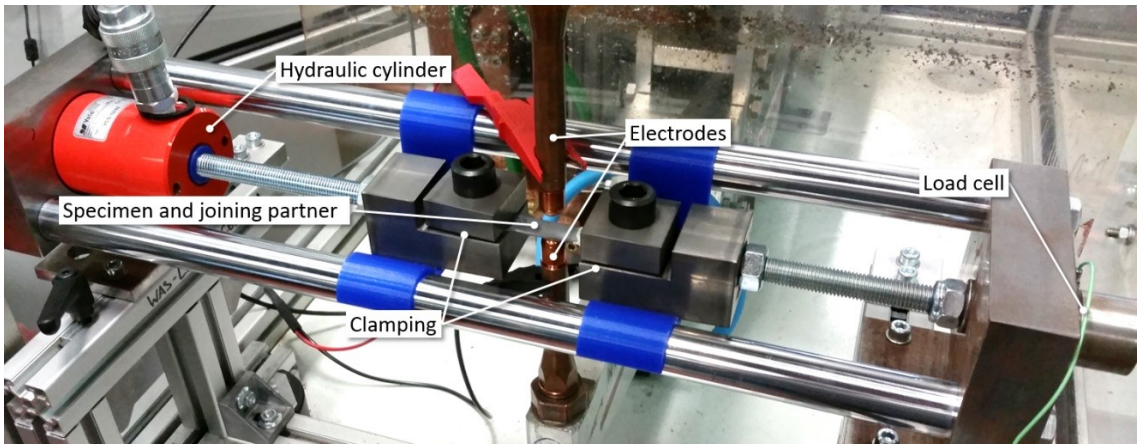

Figure 1: Experimental setup of welding under external load procedure

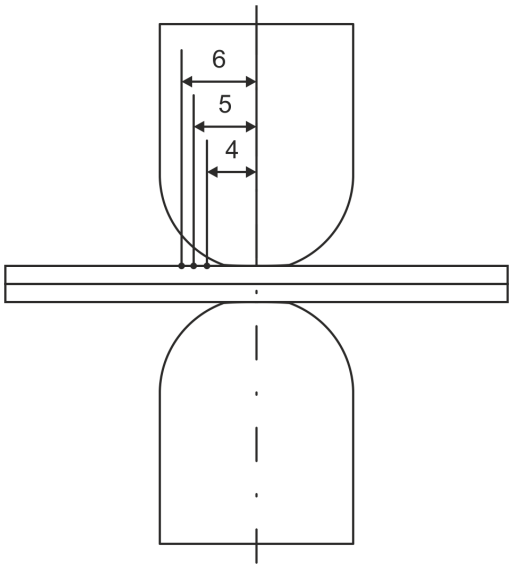

Figure 2: Location of thermocouples for temperature history measurements

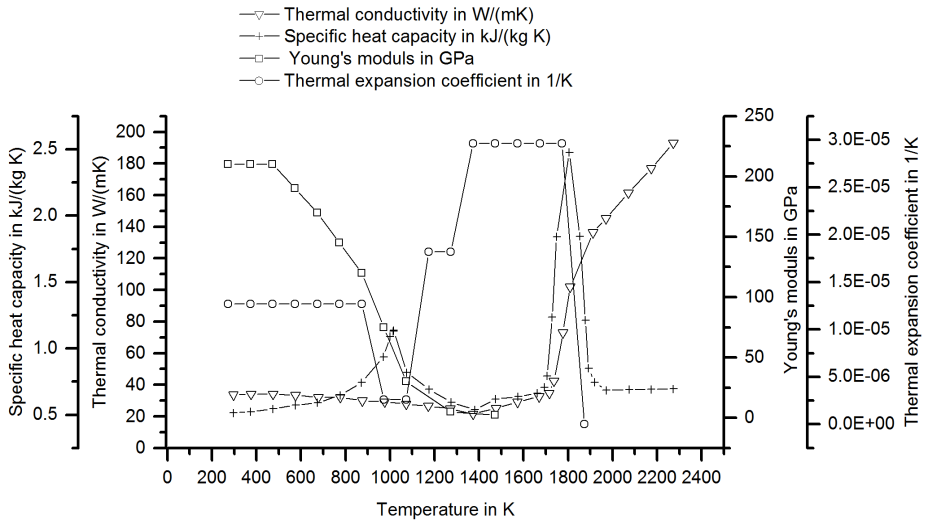

Figure 3: Thermo-physical parameters for DP1000 according to Schwenk [26]

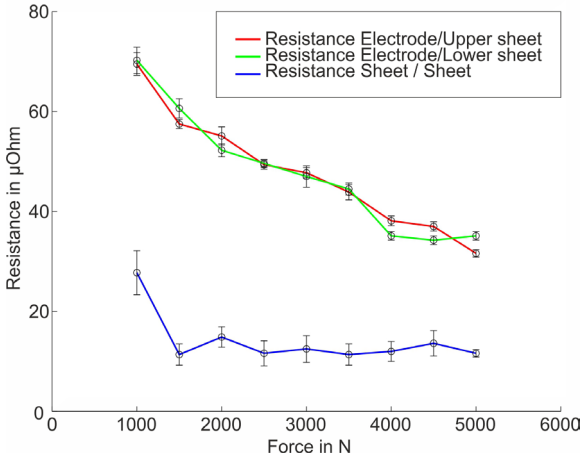

Figure 4: Measured contact resistances between sheets and between electrode and sheet at various electrode forces

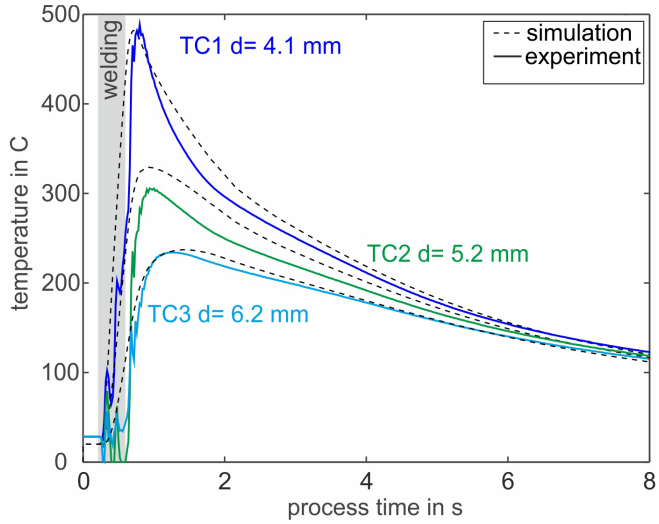

Figure 5: Temperature history of welding process, comparison of experiment and simulation (d=distance to weld center)

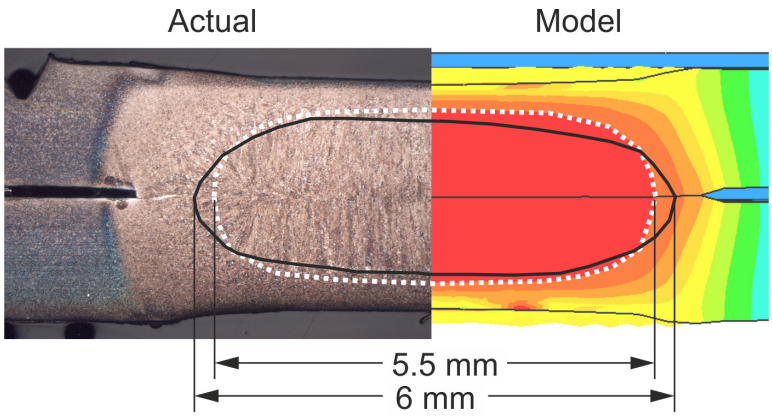

Figure 6: Actual and simulated weld nugget size for validation

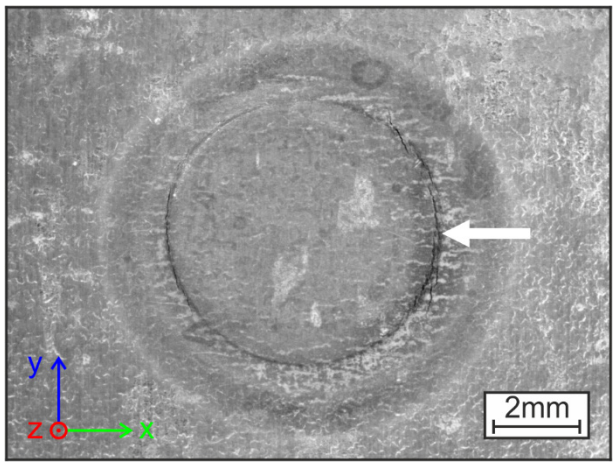

Figure 7: Top view of spot weld with typical location of LME occurrence

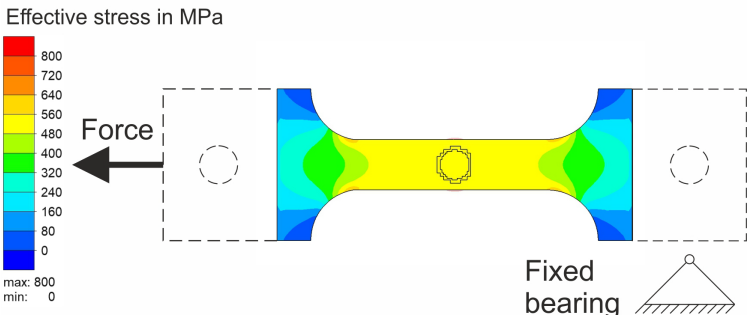

Figure 8: Simulation model of sample with uniaxial pre-stress

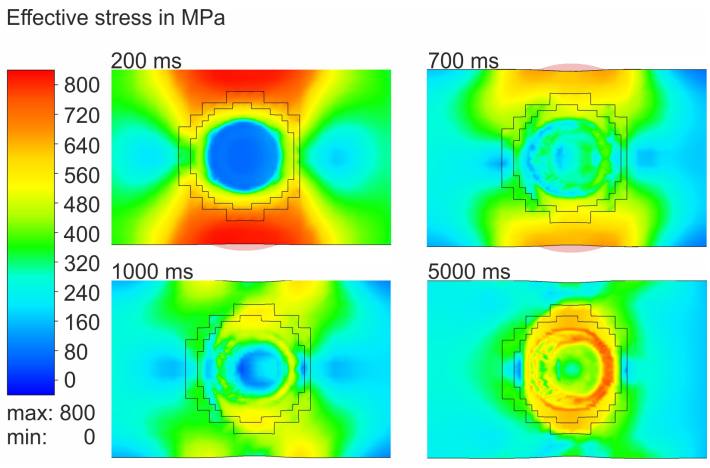

Figure 9: Effective stress field during welding under external load, top view

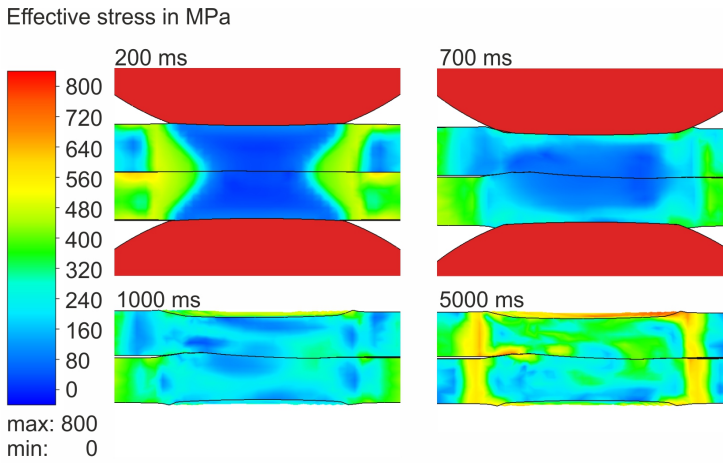

Figure 10: Effective stress field during welding under external load, cross section

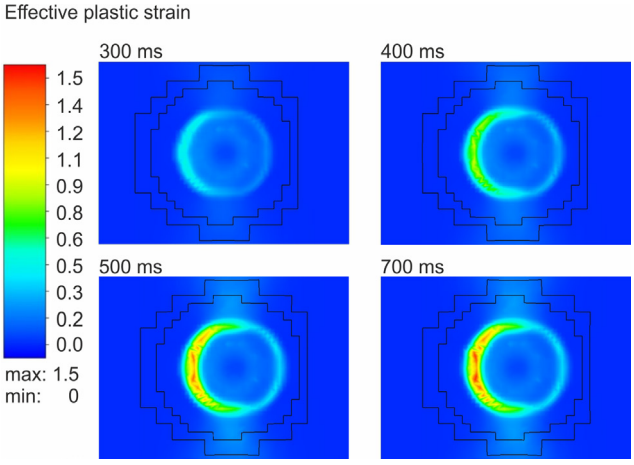

Figure 11: Effective plastic strain field during welding under external load, top view

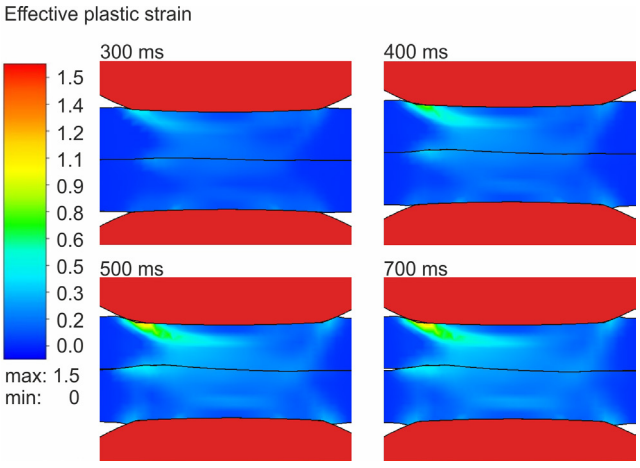

Figure 12: Effective plastic strain field during welding under external load, cross section

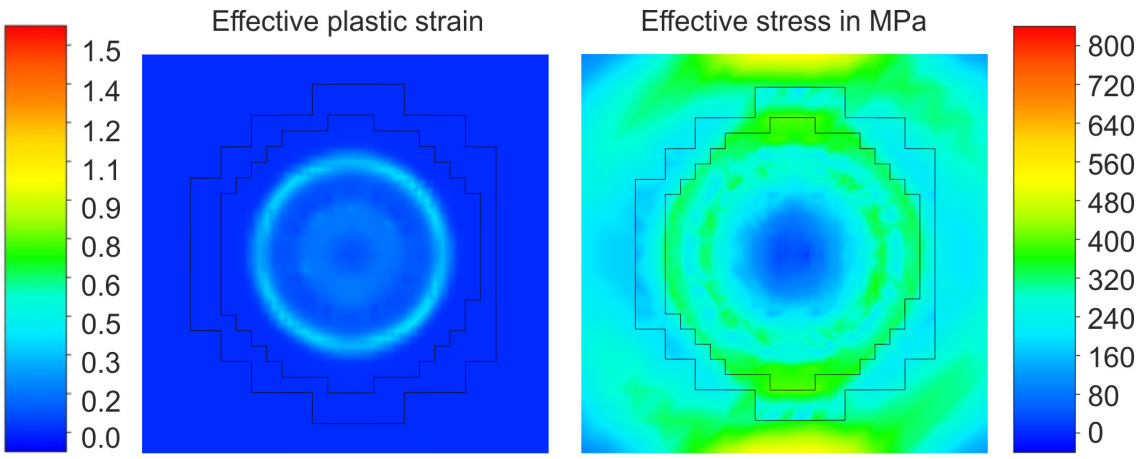

Figure 13: Effective plastic strain (left) and effective stress (right) at the end of welding time (700 ms), top view

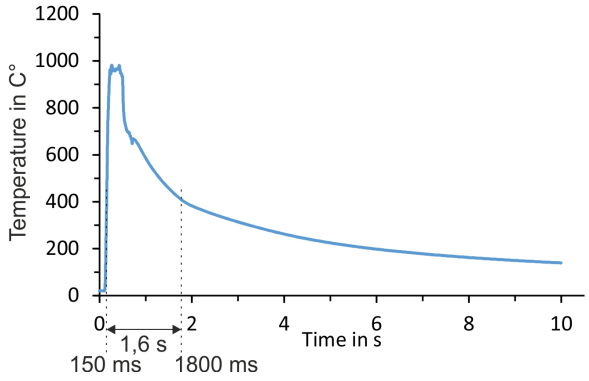

Figure 14: Simulated temperature over time on surface in electrode indentation area

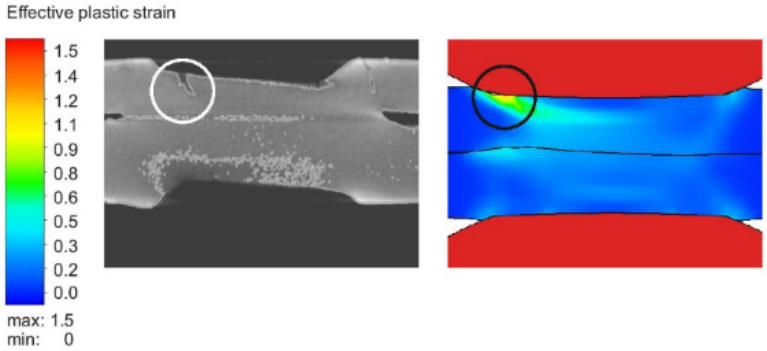

Figure 15: Effective plastic strain at 700ms in cross section compared to cross section view extracted from CT scan

Figure captions

Figure 1: Experimental setup of welding under external load procedure

Figure 2: Location of thermocouples for temperature history measurements

Figure 3: Thermo-physical parameters for DP1000 according to Schwenk [26]

Figure 4: Measured contact resistances between sheets and between electrode and sheet at various electrode forces

Figure 5: Temperature history of welding process, comparison of experiment and simulation (d=distance to weld center)

Figure 6: Actual and simulated weld nugget size for validation

Figure 7: Top view of spot weld with typical location of LME occurrence

Figure 8: Simulation model of sample with uniaxial pre-stress

Figure 9: Effective stress field during welding under external load, top view

Figure 10: Effective stress field during welding under external load, cross section

Figure 11: Effective plastic strain field during welding under external load, top view

Figure 12: Effective plastic strain field during welding under external load, cross section

Figure 13: Effective plastic strain (left) and effective stress (right) at the end of welding time (700 ms), top view

Figure 14: Simulated temperature over time on surface in electrode indentation area

Figure 15: Effective plastic strain at 700ms in cross section compared to cross section view extracted from CT scan

Biographical note

Julian Frei (M.Sc.) studied production engineering at the Technical University of Berlin. He graduated in 2014, performing research and writing his thesis at the Department of Materials Science and Engineering of the Ohio State University. Since his graduation, he is working as a research associate at the Department of Joining and Coating Technology of the Fraunhofer Institute for Production Systems and Design Technology IPK in Berlin.

Max Biegler (M.Sc.) finished his studies in mechanical engineering at Technical University of Munich in 2015. He is currently working as a research associate at Fraunhofer IPK with focus on numerical modelling of welding processes.

Univ.-Prof. Dr.-Ing. Michael Rethmeier graduated in 2003 at the Technical University Carolo Wilhelmina Braunschweig in Mechanical Engineering. Before joining the Technical University of Berlin (TUB) and the Federal Institute for Materials Research and Testing (BAM) in 2007, he worked at the Volkswagen AG. Currently, he is head of department 'Welding Technologies' (BAM), the field of 'Joining Technologies' at the Institute for Machine Tools and Factory Management (TUB) and the department of 'Joining and Coating Technology' (Fraunhofer IPK).

Christoph Böhne (M.Sc.) finished his studies in mechanical engineering at the University of Paderborn in 2017. Since then, he is working as a research associate within the work group 'thermal joining' with a focus on resistance spot welding at the Laboratory for materials and joining technology (LWF®).

Prof. Dr.-Ing. Gerson Meschut – is the head of the Laboratory for materials and joining technology (LWF®) at the University of Paderborn. After finishing his studies in Mechanical Engineering at the University of Paderborn and working at the LWF® as a research associate as well as a chief engineer, he graduated with distinction in 1998. In early 2000 he began working in corporate research at Volkswagen AG. He was the CTO of Wilhelm Böllhoff GmbH & Co. from 2005 to 2011, when he accepted the chair at the University of Paderborn.